

New Steganalytic Features for Spatial Image Steganography Based on Derivative Filters and Threshold LBP Operator

Bin Li[✉], Senior Member, IEEE, Zhongpeng Li, Shijun Zhou,
Shunquan Tan[✉], Senior Member, IEEE, and Xiaoling Zhang

Abstract—The standard local binary pattern (LBP) operator shows its versatility in performing image classification-related tasks, including texture analysis, object recognition, and steganalysis. However, a conventional well-designed scheme utilizing LBP operator and histogram-based features does not have obvious advantage when compared with the well-known steganalytic scheme spatial rich model (SRM). In this paper, we propose an adapted LBP version, called threshold LBP (TLBP), to reveal the artifacts caused by data embedding. In the proposed steganalytic scheme, the TLBP operation is performed on residual images which are obtained by using a set of high-order derivative filters to capture intricate relationships among pixels. After performing TLBP operation, second order co-occurrence matrix features are formed and then processed with aggregation and non-linear mapping for boosting feature effectiveness. Experimental results show that the proposed TLBP features prevail over SRM features under various steganographic conditions.

Index Terms—Steganalysis, threshold local binary pattern, derivative filter, co-occurrence matrix feature.

I. INTRODUCTION

STEGANOGRAPHY is a technique for covert communication by concealing information in innocuous looking cover objects [1]. Applying the strategies of minimizing distortion to reduce the deviation caused by stego noise [2]–[9], together with the effective steganographic coding schemes [10]–[12], modern image steganography has attracted considerably

Manuscript received April 13, 2017; revised September 5, 2017 and November 16, 2017; accepted November 26, 2017. Date of publication December 6, 2017; date of current version January 29, 2018. This work was supported in part by NSFC under Grant 61572329, Grant U1636202, and Grant 61772349, and in part by the Shenzhen Research and Development Program under Grant JCYJ20160328144421330. The associate editor coordinating the review of this manuscript and approving it for publication was Dr. Andrew D. Ker. (*Corresponding author: Bin Li*)

B. Li is with the College of Information Engineering, Shenzhen University, Shenzhen 518060, China, also with the Guangdong Key Laboratory of Intelligent Information Processing, Shenzhen 518060, China, and also with the Shenzhen Key Laboratory of Media Security, Shenzhen 518060, China (e-mail: libin@szu.edu.cn).

Z. Li, S. Zhou, and X. Zhang are with the College of Information Engineering, Shenzhen University, Shenzhen 518060, China (e-mail: lizhongpeng@email.szu.edu.cn; 2160130416@email.szu.edu.cn; 2014130049@email.szu.edu.cn).

S. Tan is with the College of Computer Science and Software Engineering, Shenzhen University, Shenzhen 518060, China, and also with the Shenzhen Key Laboratory of Media Security, Shenzhen 518060, China (e-mail: tansq@szu.edu.cn).

Color versions of one or more of the figures in this paper are available online at <http://ieeexplore.ieee.org>.

Digital Object Identifier 10.1109/TIFS.2017.2780805

interest in recent years. To detect whether an image contains hidden data, the prevailing trend for steganalysis is to use machine-learning classifiers [13]–[18] operating on high-dimensional features. The features can be either extracted in a hand-crafted manner [19]–[25], or automatically learned by deep convolutional neural networks [15]–[18].

The most popular hand-crafted features are extracted from rich models [19]–[24], out of which the SRM (spatial rich model) scheme [19] is the *de facto* standard approach for evaluating the security of spatial steganography. In SRM feature extraction framework, an image is firstly filtered by a set of high-pass filters to generate residual images. Then, joint distribution models of quantized residuals are obtained by computing the fourth order co-occurrence matrices. Finally, steganalytic features are obtained by merging elements in the co-occurrence matrices. A set of linear and non-linear high-pass filters with different shapes and orientations, together with several residual quantization steps, are applied to increase model diversity. Therefore, intricate high-order relationships among pixels can be modeled to quantify steganographic anomalies. If selection-channel side information is available [21], better performance can be expected.

As an alternative, features used for texture classification, such as local linear transform [26] and local binary pattern (LBP) [25], [27], [28], are helpful in detecting perturbations of micro-patterns in stego images. Among them, LBP features, which can be used for describing local structure changes, seem to be very promising. Shi *et al.* [25] proposed to use the histograms of LBP images as steganalytic features (named as LBP-HIST in this paper). However, the standard definition of LBP [29] used in LBP-HIST does not consider specific distortion characteristics resulting from data embedding in the binarization stage. As a consequence, the advantage of LBP may not be fully exploited, which results in its inferior performance compared to SRM.

Recently, deep learning attracted attentions of the steganalysis research community [15]–[18], [30]. Tan and Li [15] showed the resemblance between SRM framework and CNN (convolutional neural network) structure. Qian *et al.* [16] and Xu *et al.* [17] respectively presented a CNN structure designed for steganalysis. However, the study of deep-learned features is still in its infancy. Although some operations such as forming histogram can be simulated by specially designed

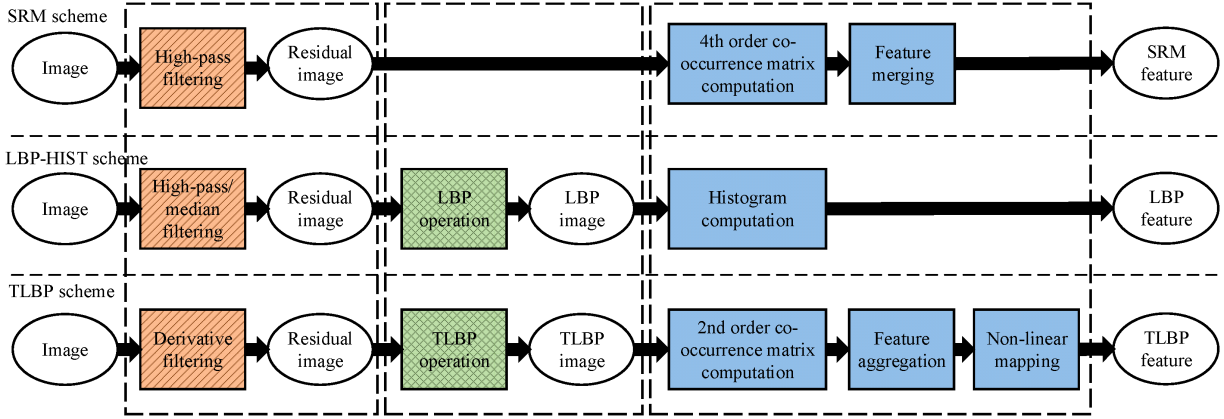


Fig. 1. The feature extraction flows for SRM, LBP-HIST, and the proposed TLBP scheme.

network layers [31], recent studies [18] also suggest that some important operations from the SRM framework, such as truncation and quantization, cannot be effectively learned by deep networks. As a result, it is still significant to improve hand-crafted steganalytic features.

In this paper, we propose a new set of steganalytic features based on an extended version of LBP that takes steganography-specific image artifacts into consideration in the binarization process. As shown in Fig. 1, with parallel comparison to SRM and LBP-HIST, the new feature extraction method contains three phases. First, in order to capture intricate relationships among pixels, a set of high-order derivative filters are proposed to generate residual images. This stage resembles the high-pass filtering and/or median filtering used in SRM and LBP-HIST. The derivative filters with directionality can be used not only for filtering out the image content but also for evaluating the weak perturbation caused by stego noise. Second, an extension of LBP, called *Threshold LBP* (TLBP), is introduced to capture the deviation caused by steganography in residual images. Such a stage, by generating TLBP images from residual images, is not applied in SRM feature extraction process. Compared to the conventional LBP operator, the proposed TLBP operator is more sensitive to embedding changes. Third, features from second-order co-occurrence matrices are computed from TLBP images. They are aggregated and non-linearly mapped to boost feature effectiveness. Compared to histograms utilized in LBP-HIST for statistics description, co-occurrence matrices are more versatile. The feature aggregation step reduces feature dimension and enhances feature robustness. Since the proposed scheme computes co-occurrence matrices from TLBP images that do not have signs, sign symmetrical merging used in SRM may not be applicable. We only use the directional symmetry property of co-occurrence matrix for aggregation. The non-linear mapping step is an integrated part of the proposed feature extraction method for reducing the high dynamic range of features.

The contributions of this work are summarized as follows.

- 1) The proposed TLBP operator can effectively work on residual images to capture steganographic deviation. Our analysis shows that the proposed TLBP operator

is more sensitive to embedding changes than the previous LBP operators [25], [29]. Compared to the SRM framework, a major difference is that TLBP is used after obtaining residual images and before forming co-occurrence matrices, as shown in Fig. 1. Since TLBP is able to characterize the magnitude relationship between the central element and its neighbors in all directions, it has better modeling capability than directly using co-occurrences that are computed along a fixed direction.

- 2) A novel compact set of derivative filters are introduced for generating residual images. In contrast to previous methods which used a large number of unsystematically designed high-pass filters, the proposed method utilize derivative filters that have clear mathematical meaning and can efficiently satisfy the requirement to evaluate the intricate relationships among neighboring pixels.
- 3) The proposed TLBP features achieve good steganalytic performance under various conditions. When analyzing the effectiveness of features with Laplacian score [32], the proposed features consistently outperform both SRM and LBP-HIST features under the same dimensionality. The TLBP features are comparable to maxSRM features equipped with selection channel information in some cases. When combined with SRM/maxSRM features, better performance can be obtained.

The rest of this paper is structured as follows. In Section II, we present the fundamentals of LBP to make this paper self-contained. The proposed TLBP features are studied from Section III to Section V, where Section III describes the derivative filters for obtaining residual images, Section IV presents the TLBP operator, and then Section V explains the detailed feature extraction steps. Experimental results are demonstrated in Section VI. Finally, we conclude the paper in Section VII. Our implementation codes can be downloaded from <http://media-sec.szu.edu.cn/couch/uploads/file/TLBP-v1.0.rar>.

II. FUNDAMENTALS OF LOCAL BINARY PATTERN

A. Definition of LBP

LBP [29] is a descriptor initially designed for texture classification, which evaluates the sign relation between the

central pixel and its neighboring pixels in a given distance. Specifically, for a given center pixel I_c and its neighboring pixels I_p ($p \in \{0, \dots, P-1\}$) on a circle of radius R ($R > 0$), the LBP operator is defined as

$$LBP_{P,R} = \sum_{p=0}^{P-1} s(I_p - I_c) \cdot 2^p, \quad (1)$$

where $s(\cdot)$ is the binarization function defined as

$$s(x) = \begin{cases} 1, & x \geq 0, \\ 0, & x < 0. \end{cases} \quad (2)$$

The P pixels in the neighborhood can be selected in a clockwise manner and the $LBP_{P,R}$ operator produces 2^P codes.

B. LBP Extensions

There are numerous LBP variants in the literatures, such as LTP (local ternary pattern) [33], LDP (local derivative pattern) [34], ILBP (improved local binary pattern) [35]. They have been adopted for different purposes, including texture analysis, object recognition, image retrieval, etc.

A popular extension is called *rotation invariant uniform LBP* ($LBP_{P,R}^{riu2}$) [36], which is a combination of *uniform LBP* ($LBP_{P,R}^{u2}$) and *rotation invariant LBP* ($LBP_{P,R}^{ri}$). A quantity measuring the bitwise 0/1 transition in the binary representation of LBP codes is defined as

$$\begin{aligned} U(LBP_{P,R}) = & |s(I_{P-1} - I_c) - s(I_0 - I_c)| \\ & + \sum_{p=0}^{P-1} |s(I_p - I_c) - s(I_{p-1} - I_c)|. \end{aligned} \quad (3)$$

If $U(LBP_{P,R}) \leq 2$, the corresponding LBP code is considered as *uniform*. There are $P(P-1)+2$ uniform patterns and the rest can be regarded as belonging to a single type called *non-uniform pattern*. The $LBP_{P,R}^{u2}$ operator is used to distinguish the LBP codes whose 0/1 transition is limited to at most two times. It produces $P(P-1)+3$ codes.

In order to achieve rotation invariance, $LBP_{P,R}^{ri}$ is defined as

$$LBP_{P,R}^{ri} = \min \{ROR(LBP_{P,R}, k) | k = 0, \dots, P-1\}, \quad (4)$$

where $ROR(b, k)$ executes a circular bit-wise shift on b by k bits. A rotation invariant uniform LBP operator can be defined as

$$LBP_{P,R}^{riu2} = \begin{cases} \sum_{p=0}^{P-1} s(I_p - I_c), & \text{if } U(LBP_{P,R} \leq 2), \\ P+1, & \text{otherwise.} \end{cases} \quad (5)$$

The $LBP_{P,R}^{riu2}$ operator produces $P+2$ codes, which greatly decreases the dimensionality of $LBP_{P,R}$ codes.

C. LBP Features for Steganalysis

Shi *et al.* presented an effective LBP feature extraction scheme (LBP-HIST) for steganalysis [25], as shown in Fig. 1. In this scheme, residual images are first obtained by using various kinds of predictors, including median filters and high

pass filters based on Markov neighborhoods and Law's masks. Then, $LBP_{8,1}^{u2}$, $LBP_{8,2}^{u2}$, $LBP_{8,3}^{u2}$, and $LBP_{8,1}$ are used to obtain LBP images from the residual images. Finally, histograms of the LBP images are concatenated to form a feature vector of 22,153 dimensions. It achieves a satisfactory performance in detecting stego images from HUGO [2]. However, the LBP operators designed in such a scheme do not fully exploit the embedding impacts caused by steganographic modification, referred to the analysis in Section IV. Besides, histogram is a kind of first-order statistic, whose modeling power is limited for data containing mutual dependencies. The fact that the current LBP-HIST scheme is not optimized for steganalysis motivates us to seek more powerful dedicated adaption.

III. OBTAINING RESIDUAL IMAGES WITH DERIVATIVE FILTERS

In order to enhance undetectability, modern content-adaptive steganography makes more changes in textual regions and less changes in smooth regions. Besides, stego signals in an image are weak compared to image content. Therefore, it is common to strengthen stego signals by filtering out image content, and then compute the statistics from the resultant residual images. In previous studies, various kinds of high-pass filters have been used, but most of them are unsystematically designed.

In this work, we use directional derivative filters, which have clear mathematical meaning, to explore the intricate relationships among pixels. It is known that some manipulations in the image processing pipeline, such as bilinear/bicubic resampling with anti-aliasing, can smooth local regions and therefore introduce different extents of correlation in images. Derivatives are often used to measure the instantaneous rate of change in signals. Therefore, the derivative filters applied in our scheme can, on the one hand, be served as the high-pass filter to filter out the image contents, and on the other hand, be used to evaluate the weak perturbation caused by stego noise.

A. Definition of Derivative Filters

For an image $f(x, y)$, where x and y denotes the spatial coordinates, the first and the n -th partial derivative in the horizontal direction can respectively be defined as

$$\frac{\partial f(x, y)}{\partial x} = f(x, y) - f(x+1, y), \quad (6)$$

and

$$\frac{\partial^n f(x, y)}{\partial x^n} = \frac{\partial^{n-1} f(x, y)}{\partial x^{n-1}} - \frac{\partial^{n-1} f(x, y)}{\partial (x+1)^{n-1}}. \quad (7)$$

Let $D_{n,m}$ denote the derivative filter of the order n and m respectively in the horizontal and the vertical direction. It can be defined as

$$\begin{aligned} & \frac{\partial^m}{\partial y^m} \left(\frac{\partial^n f(x, y)}{\partial x^n} \right) \\ &= \frac{\partial^{m-1}}{\partial y^{m-1}} \left(\frac{\partial^n f(x, y)}{\partial x^n} \right) - \frac{\partial^{m-1}}{\partial (y+1)^{m-1}} \left(\frac{\partial^n f(x, y)}{\partial x^n} \right). \end{aligned} \quad (8)$$

TABLE I
PADDED AND ROTATED VERSION OF DERIVATIVE FILTERS AND THE RESULTANT LINEAR AND NON-LINEAR RESIDUAL IMAGES

Class	Padded filter	Rotated example	Linear residuals	Non-linear residuals
C#1	$\tilde{\mathbf{D}}_{1,0}^{(0^\circ)} = \begin{bmatrix} 0 & 0 & 0 \\ 1 & -1 & 0 \\ 0 & 0 & 0 \end{bmatrix}$	$\tilde{\mathbf{D}}_{1,0}^{(45^\circ)} = \begin{bmatrix} 1 & 0 & 0 \\ 0 & -1 & 0 \\ 0 & 0 & 0 \end{bmatrix}$	$R_{\tilde{\mathbf{D}}_{1,0}^{(0^\circ)}}, R_{\tilde{\mathbf{D}}_{1,0}^{(90^\circ)}}$	$R_{\tilde{\mathbf{D}}_{1,0}^{max}}, R_{\tilde{\mathbf{D}}_{1,0}^{min}}$
	$\tilde{\mathbf{D}}_{3,0}^{(0^\circ)} = \begin{bmatrix} 0 & 0 & 0 & 0 & 0 \\ 0 & 0 & 0 & 0 & 0 \\ 1 & -3 & 3 & -1 & 0 \\ 0 & 0 & 0 & 0 & 0 \\ 0 & 0 & 0 & 0 & 0 \end{bmatrix}$	$\tilde{\mathbf{D}}_{3,0}^{(45^\circ)} = \begin{bmatrix} 1 & 0 & 0 & 0 & 0 \\ 0 & -3 & 0 & 0 & 0 \\ 0 & 0 & 3 & 0 & 0 \\ 0 & 0 & 0 & -1 & 0 \\ 0 & 0 & 0 & 0 & 0 \end{bmatrix}$	$R_{\tilde{\mathbf{D}}_{3,0}^{(0^\circ)}}, R_{\tilde{\mathbf{D}}_{3,0}^{(90^\circ)}}$	$R_{\tilde{\mathbf{D}}_{3,0}^{max}}, R_{\tilde{\mathbf{D}}_{3,0}^{min}}$
C#2	$\tilde{\mathbf{D}}_{2,0}^{(0^\circ)} = \begin{bmatrix} 0 & 0 & 0 \\ 1 & -2 & 1 \\ 0 & 0 & 0 \end{bmatrix}$	$\tilde{\mathbf{D}}_{2,0}^{(45^\circ)} = \begin{bmatrix} 1 & 0 & 0 \\ 0 & -2 & 0 \\ 0 & 0 & 1 \end{bmatrix}$	$R_{\tilde{\mathbf{D}}_{2,0}^{(0^\circ)}}, R_{\tilde{\mathbf{D}}_{2,0}^{(90^\circ)}}$	$R_{\tilde{\mathbf{D}}_{2,0}^{max}}, R_{\tilde{\mathbf{D}}_{2,0}^{min}}$
	$\tilde{\mathbf{D}}_{4,0}^{(0^\circ)} = \begin{bmatrix} 0 & 0 & 0 & 0 & 0 \\ 0 & 0 & 0 & 0 & 0 \\ 1 & -4 & 6 & -4 & 1 \\ 0 & 0 & 0 & 0 & 0 \\ 0 & 0 & 0 & 0 & 0 \end{bmatrix}$	$\tilde{\mathbf{D}}_{4,0}^{(45^\circ)} = \begin{bmatrix} 1 & 0 & 0 & 0 & 0 \\ 0 & -4 & 0 & 0 & 0 \\ 0 & 0 & 6 & 0 & 0 \\ 0 & 0 & 0 & -4 & 0 \\ 0 & 0 & 0 & 0 & 1 \end{bmatrix}$	$R_{\tilde{\mathbf{D}}_{4,0}^{(0^\circ)}}, R_{\tilde{\mathbf{D}}_{4,0}^{(90^\circ)}}$	$R_{\tilde{\mathbf{D}}_{4,0}^{max}}, R_{\tilde{\mathbf{D}}_{4,0}^{min}}$
C#3	$\tilde{\mathbf{D}}_{2,1}^{(0^\circ)} = \begin{bmatrix} -1 & 2 & -1 \\ 1 & -2 & 1 \\ 0 & 0 & 0 \end{bmatrix}$	$\tilde{\mathbf{D}}_{2,1}^{(90^\circ)} = \begin{bmatrix} 0 & 1 & -1 \\ 0 & -2 & 2 \\ 0 & 1 & -1 \end{bmatrix}$	$R_{\tilde{\mathbf{D}}_{2,1}^{(0^\circ)}}, R_{\tilde{\mathbf{D}}_{2,1}^{(90^\circ)}}$	$R_{\tilde{\mathbf{D}}_{2,1}^{max}}, R_{\tilde{\mathbf{D}}_{2,1}^{min}}$
	$\tilde{\mathbf{D}}_{4,2}^{(0^\circ)} = \begin{bmatrix} 1 & -4 & 6 & -4 & 1 \\ -2 & 8 & -12 & 8 & -2 \\ 1 & -4 & 6 & -4 & 1 \\ 0 & 0 & 0 & 0 & 0 \\ 0 & 0 & 0 & 0 & 0 \end{bmatrix}$	$\tilde{\mathbf{D}}_{4,2}^{(90^\circ)} = \begin{bmatrix} 0 & 0 & 1 & -2 & 1 \\ 0 & 0 & -4 & 8 & -4 \\ 0 & 0 & 6 & -12 & 6 \\ 0 & 0 & -4 & 8 & -4 \\ 0 & 0 & 1 & -2 & 1 \end{bmatrix}$	$R_{\tilde{\mathbf{D}}_{4,2}^{(0^\circ)}}, R_{\tilde{\mathbf{D}}_{4,2}^{(90^\circ)}}$	$R_{\tilde{\mathbf{D}}_{4,2}^{max}}, R_{\tilde{\mathbf{D}}_{4,2}^{min}}$
C#4	-	-	$R_{\mathbf{D}_{1,1}}, R_{\mathbf{D}_{2,2}}, R_{\mathbf{D}_{3,3}}, R_{\mathbf{D}_{4,4}}$	-

As the mix partial derivative is separable, $\mathbf{D}_{n,m}$ can be obtained by convolving $\mathbf{D}_{n,0}$ with $\mathbf{D}_{0,m}$. For example,

$$\begin{aligned} \mathbf{D}_{2,1} &= \mathbf{D}_{2,0} \otimes \mathbf{D}_{0,1} = [-1 \ 2 \ -1] \otimes \begin{bmatrix} 1 \\ -1 \end{bmatrix} \\ &= \begin{bmatrix} -1 & 2 & -1 \\ 1 & -2 & 1 \end{bmatrix}. \end{aligned} \quad (9)$$

As studied in [19], pixel dependencies decrease with increasing distance between pixels. We use partial derivatives up to the fourth order to effectively characterize the pixel relation within five pixels along a specified direction. When a mixed partial derivative filter is used, and the TLBP operation and co-occurrence matrix are involved in the later feature extraction stages, relation among more pixels can be taken into consideration. Ten derivative filters, divided into four classes, are adopted as basic filters and enumerated as follows:

- C#1: $\mathbf{D}_{1,0}$ and $\mathbf{D}_{3,0}$.
- C#2: $\mathbf{D}_{2,0}$ and $\mathbf{D}_{4,0}$.
- C#3: $\mathbf{D}_{2,1}$ and $\mathbf{D}_{4,2}$.
- C#4: $\mathbf{D}_{1,1}$, $\mathbf{D}_{2,2}$, $\mathbf{D}_{3,3}$, and $\mathbf{D}_{4,4}$.

A residual image, obtained by convolving an image with a filter \mathbf{D} , is denoted as $R_{\mathbf{D}}$.

B. Padding and Rotation

Note that the shape of filters in C#1 to C#3 is not square. In order to explore pixel relationships along different directions, padded and rotated filters are used. Filters in C#4 remain unchanged due to their square shape and central symmetry property.

$\mathbf{D}_{1,0}$, $\mathbf{D}_{2,0}$, and $\mathbf{D}_{2,1}$ are padded to 3×3 , while $\mathbf{D}_{3,0}$, $\mathbf{D}_{4,0}$, and $\mathbf{D}_{4,2}$ are padded to 5×5 . The original derivative filter in C#1 is located in the left middle part of the full 3×3

or 5×5 matrix (see Table I for example). Analogously, filters in C#2 are located in the middle, and filters in C#3 are located in the upper part. Let $\tilde{\mathbf{D}}_{n,m}^{(r \cdot 45^\circ)}$ denote a rotated and padded version of $\mathbf{D}_{n,m}$ with rotation angle of $r \cdot 45^\circ$, measured in a clockwise manner. We use eight rotated versions ($r \in \{0, 1, \dots, 7\}$) in C#1, four rotated versions ($r \in \{0, 1, 2, 3\}$) in C#2, and four rotated versions ($r \in \{0, 2, 4, 6\}$) in C#3.

C. Non-Linear Filtering

In order to introduce non-linearity, “max” and “min” operators are applied, as done in [19]. The “max” (or “min”) operator computes the maximum (or minimum) values among the residual images obtained by convolving an image with padded and rotated versions of each basic filter in C#1 to C#3. The output residual is designated as $R_{\mathbf{D}}^{max}$ (or $R_{\mathbf{D}}^{min}$). For example,

$$R_{\tilde{\mathbf{D}}_{4,2}}^{max} = \max \left\{ R_{\tilde{\mathbf{D}}_{4,2}^{(0^\circ)}}, R_{\tilde{\mathbf{D}}_{4,2}^{(90^\circ)}}, R_{\tilde{\mathbf{D}}_{4,2}^{(180^\circ)}}, R_{\tilde{\mathbf{D}}_{4,2}^{(270^\circ)}} \right\}, \quad (10)$$

$$R_{\tilde{\mathbf{D}}_{4,2}}^{min} = \min \left\{ R_{\tilde{\mathbf{D}}_{4,2}^{(0^\circ)}}, R_{\tilde{\mathbf{D}}_{4,2}^{(90^\circ)}}, R_{\tilde{\mathbf{D}}_{4,2}^{(180^\circ)}}, R_{\tilde{\mathbf{D}}_{4,2}^{(270^\circ)}} \right\}. \quad (11)$$

Table I shows some examples of padded and rotated filters, and enumerates linear residual images and non-linear residual images for each filter class. In total, 16 linear residual images and 12 non-linear residual images are obtained in the proposed scheme.

D. Residual Quantization and Truncation

In order to increase feature effectiveness, residual images are quantized and truncated as

$$[R_{\mathbf{D}}]_{q,M} = \text{trunc}_M \left(\text{round} \left(\frac{R_{\mathbf{D}}}{q} \right) \right), \quad (12)$$

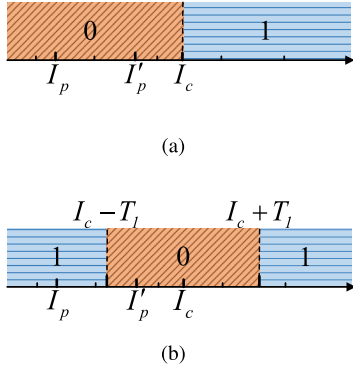


Fig. 2. Illustration of the different binarization process between LBP and TLBP. I_c is the central pixel, and I_p is an adjacent pixel smaller than I_c . I'_p is a stego version of I_p by increasing its value, but I'_p is still smaller than I_c . In the LBP scheme (a), the binary code remain unchanged. In the TLBP scheme (b), the binary code is changed from 1 to 0. (a) Binarization of LBP. (b) Binarization of TLBP.

where the quantization step q takes the maximum element of the filter \mathbf{D} that is used to generate the residual image $R_{\mathbf{D}}$. The truncation operation is defined as

$$\text{trunc}_M(x) = \begin{cases} x, & x \in [-M, M], \\ \text{sign}(x) \cdot M, & \text{otherwise}, \end{cases} \quad (13)$$

where the truncation threshold is set to $M = 2$. In our scheme, both unquantized residual images and quantized-and-truncated residual images are used for generating features, as described in the following subsections.

IV. BINARIZATION WITH THE TLBP OPERATOR

In contrast to the SRM framework [19] which directly utilizes the statistics of residuals as features, the LBP-HIST scheme [25] further processes residual images to yield LBP images. As defined in (2) and illustrated in Fig. 2(a), the binarization function of the standard LBP operator only focuses on whether an adjacent pixel I_p is larger or smaller than the central pixel I_c . In other words, only the sign of their difference is considered. However, ignoring the magnitude has disadvantages in steganalysis. As the disturbance of stego noise is slight, such as the stego signal I'_p illustrated in Fig. 2(a), it is likely that the sign of $I'_p - I_c$ remains unaffected but the magnitude is changed. The current binarization function is insensitive to such changes. The binarization operation is applied to residual images in our case, which makes the problem more apparent because residuals contain both positive and negative values. To address such a problem, we define an adapted LBP operator, in which the binarization process takes the magnitude relationship into account by using a pre-defined threshold.

A. Definition of TLBP

The proposed Threshold LBP (TLBP) operator is defined as

$$\text{TLBP}_{P,R,T} = \sum_{p=0}^{P-1} s_T(I_p - I_c) \cdot 2^p, \quad (14)$$

where

$$s_T(x) = \begin{cases} 1, & |x| \geq T, \\ 0, & |x| < T. \end{cases} \quad (15)$$

The binarization process in (14) aims to evaluate whether the distance between I_p and I_c is less than T . The change caused by data embedding can be revealed by the change of distance between two neighboring residual image pixels, and thus captured by TLBP code. Hence, it is possible for TLBP operator to take effect when LBP cannot, as shown in Fig. 2(b). When replacing the binarization function $s(x)$ in (3) and that in (5) by (15), respectively, we can obtain an uniform TLBP operator $\text{TLBP}_{P,R,T}^{u2}$ and a rotation invariant uniform TLBP operator $\text{TLBP}_{P,R,T}^{riu2}$. Note that both $\text{LBP}_{P,R}^{riu2}$ and $\text{TLBP}_{P,R,T}^{riu2}$ produce $P + 2$ codes.

B. Threshold Selection

The threshold T in (15) is vital to steganalytic performance. Let $Z = I_p - I_c$. The binarization process in (15) will transform the distribution of Z into Bernoulli distribution (0-1 distribution). We denote the random variable after binarization as \tilde{Z} . Its probability mass function (PMF) is

$$P_{\tilde{Z}}(\tilde{z}) = \begin{cases} p_0, & \tilde{z} = 0, \\ 1 - p_0, & \tilde{z} = 1, \end{cases} \quad (16)$$

where p_0 is the probability of \tilde{Z} being zero. For unquantized residual images, denote the probability density function (PDF) of Z as $f_Z(z)$. We have

$$p_0 = P\{|Z| < T\} = \int_{-T}^T f_Z(z) dz, \quad (0 < T < +\infty). \quad (17)$$

For quantized and truncated images, denote the PMF of Z as $P_Z(z)$. We have

$$p_0 = P\{|Z| < T\} = \sum_{z=-T}^T P_Z(z), \quad (0 < T \leq 2M). \quad (18)$$

As shown in (17) and (18), p_0 is related to the threshold T . Once a cover image and its corresponding stego image are given, the PDFs/PMFs of $Z^{(c)}$ and $Z^{(s)}$ are known. It is possible to obtain the optimal value of T that can maximize the performance of the TLBP operator in distinguishing cover and stego images by maximizing the Kullback-Leibler divergence between two distributions ($P_{\tilde{Z}^{(c)}}$ and $P_{\tilde{Z}^{(s)}}$):

$$\begin{aligned} T_{opt} &= \arg \max_T D_{KL}(P_{\tilde{Z}^{(c)}} || P_{\tilde{Z}^{(s)}}) \\ &= \arg \max_T \left\{ p_0^{(c)} \log \frac{p_0^{(c)}}{p_0^{(s)}} + (1 - p_0^{(c)}) \log \frac{1 - p_0^{(c)}}{1 - p_0^{(s)}} \right\}. \end{aligned} \quad (19)$$

In practice, however, the distribution $f_{Z^{(c)}}$ for a cover image is unknown, which hinders us finding T_{opt} . Although we can assume $f_{Z^{(c)}}$ and $f_{Z^{(s)}}$ follow a specific distribution, such as the generalized Gaussian distribution, and estimate their model parameters from empirical data, the theoretical model does not fit the data well enough. In our trail experiments, we have tried several types of distribution; however, the estimation \hat{T}_{opt} is

TABLE II
THE THRESHOLD T USED FOR UNQUANTIZED RESIDUAL IMAGE

	$D_{1,0}$	$D_{2,0}$	$D_{3,0}$	$D_{4,0}$	$D_{2,1}$	$D_{4,2}$	$D_{1,1}$	$D_{2,2}$	$D_{3,3}$	$D_{4,4}$
d_{max}	1	2	3	6	2	12	1	4	9	36
α	1.4142	1.4142	1.6330	1.6330	2.0000	2.3094	2.0000	2.0000	2.6667	2.6667
T	1	2	4	9	4	27	2	8	24	96

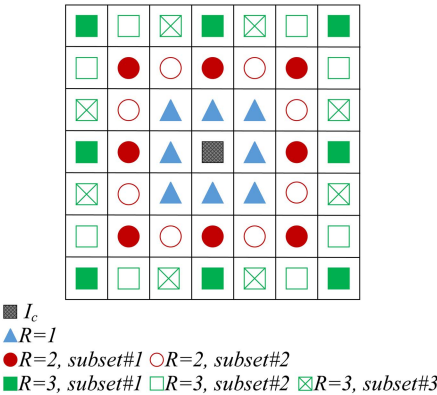


Fig. 3. The illustration of neighboring pixels of I_c to obtain TLBP images. When $R = 1$, $R = 2$, and $R = 3$, there are 8, 16, and 24 neighboring pixels, and marked with triangles, circles, and squares, respectively. The neighboring pixels with $R = 2$ and $R = 3$ are divided into 2 and 3 subsets, respectively.

often deviated from T_{opt} because of the model deviation and the diversity of cover images.

As an alternative, we set T heuristically. For quantized and truncated residual images, we use $T = M$, where M is defined in (13). For unquantized residual images, we select T according to the absolute maximum element of the corresponding derivative filter by

$$T = \lfloor \alpha \cdot d_{max} \rfloor, \quad (20)$$

where $d_{max} = \max_{i,j} |d_{i,j}|$, and $d_{i,j}$ is the (i, j) -th element in the filter $D_{m,n}$. The scaling factor α is set as

$$\alpha = \sqrt{\sum_{i,j} \left| \frac{d_{i,j}}{d_{max}} \right|}, \quad (21)$$

which can be considered as taking the square root of the summation of normalized absolute values of filter coefficients. The thresholds used in the proposed method are shown in Table II.

C. Multi-Scale Extension and Division

In order to model pixel relationship in different scales, we use several values of radius R in the operator defined in (14). The checkerboard distance (D_8 distance) is used to define the spatial distance R between I_p and I_c . When R is set to 1, 2, and 3, respectively, P equals to 8, 16, and 24. To reduce the number of LBP codes, we divide neighboring pixels of I_c with a distance of R into R subsets, as shown in Fig. 3. Therefore, six neighboring pixel sets are formed, each one with $P = 8$, and six resultant TLBP images are generated for each residual image.

TABLE III
THE CHANGE RATE BETWEEN THE TLBP/LBP COVER IMAGE AND ITS STEGO COUNTERPART BY USING S-UNIWARD (0.4 bpp)

	$\tilde{D}_{1,0}^{(0^\circ)}$	$\tilde{D}_{2,0}^{(0^\circ)}$	$\tilde{D}_{2,1}^{(0^\circ)}$	$D_{3,3}$
TLBP	0.1395	0.1476	0.1547	0.1591
LBP	0.0749	0.0895	0.1180	0.1473

In order to show the effectiveness of TLBP operator to capture steganographic modifications, we make an experiment as follows. We randomly select 100 cover images from BOSSBase 1.01 [37] and use the steganographic scheme S-UNIWARD with the payload 0.4 bit per pixel to generate stego images. Then we use four filters $\tilde{D}_{1,0}^{(0^\circ)}$, $\tilde{D}_{2,0}^{(0^\circ)}$, $\tilde{D}_{2,1}^{(0^\circ)}$, and $D_{3,3}$, to get linear residuals. Later, we use $TLBP_{P,R,T}^{riu2}$ and $LBP_{P,R}^{riu2}$ operator with $R = 1$ and $P = 8$ respectively to obtain TLBP or LBP images. Finally, we compute the change rate between the TLBP (or LBP) cover image and its stego counterpart. The change rates, defined as the ratio of the number of changed pixels to the total number of image pixels, averaged over 100 images are shown in Table III. It can be noted that TLBP images have higher change rates than LBP images, indicating that TLBP operator is more sensitive to steganographic modification.

V. FEATURE EXTRACTION

In our scheme, the $TLBP_{P,R,T}^{riu2}$ operator is used to obtain TLBP images. Therefore, the value of TLBP image elements ranges from 0 to 9. For each TLBP image, features from co-occurrence matrices are extracted, which are more powerful than the first-order histogram used in LBP-HIST [25] for describing image statistics. In order to reduce feature dimension and boost feature effectiveness, co-occurrence matrices are aggregated, and the resultant elements are non-linearly mapped. The whole feature extraction process is illustrated in Fig. 4, and detailed as follows.

A. Co-Occurrence Matrix Formation

Let $B(i, j)$ ($0 \leq i \leq U - 1, 0 \leq j \leq V - 1$) be the pixel of a TLBP image at location (i, j) . Standard second-order co-occurrence matrices are formed along horizontal, vertical, diagonal, and anti-diagonal directions as:

$$C^{\rightarrow}(k, l) = \frac{\sum_{i=0}^{U-1} \sum_{j=0}^{V-2} \delta(B(i, j) - k, B(i, j+1) - l)}{U \cdot (V - 1)}, \quad (22)$$

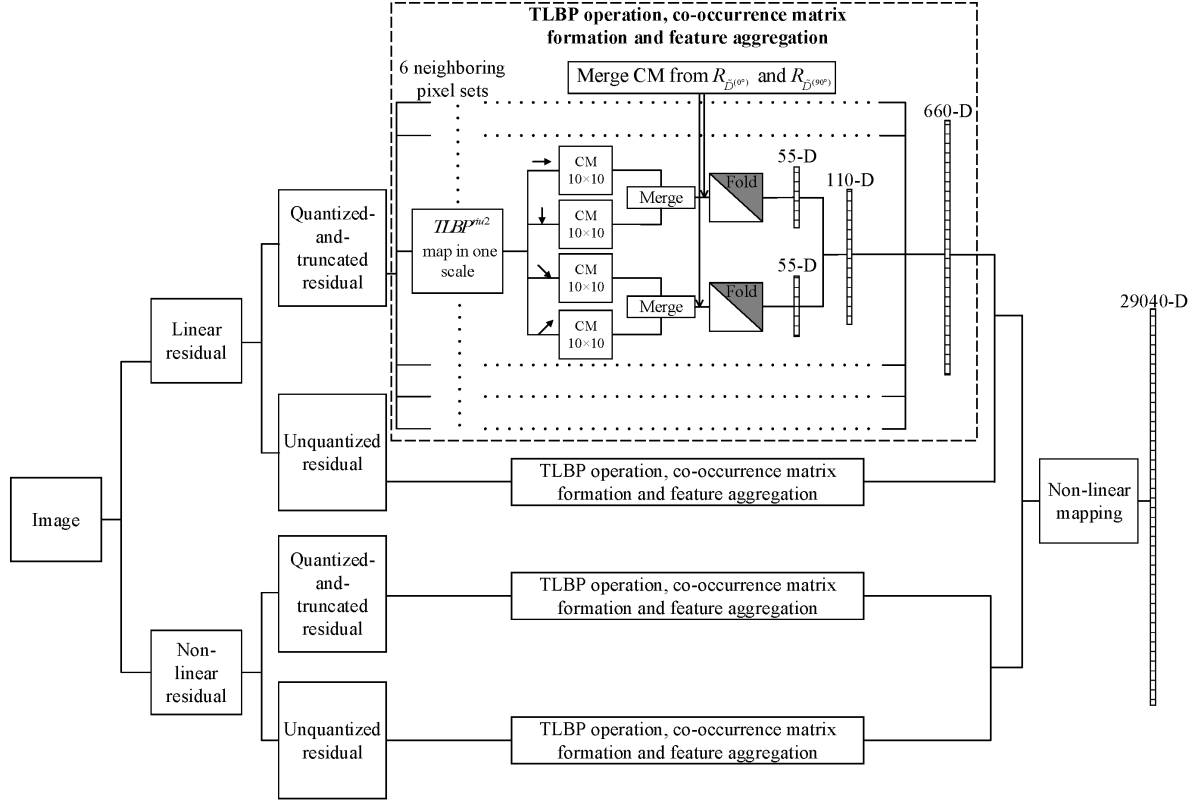


Fig. 4. The flowchart of TLBP feature extraction.

$$C^{\downarrow}(k, l) = \frac{\sum_{i=0}^{U-2} \sum_{j=0}^{V-1} \delta(B(i, j) - k, B(i+1, j) - l)}{(U-1) \cdot V}, \quad (23)$$

$$C^{\nwarrow}(k, l) = \frac{\sum_{i=0}^{U-2} \sum_{j=0}^{V-2} \delta(B(i, j) - k, B(i+1, j+1) - l)}{(U-1) \cdot (V-1)}, \quad (24)$$

$$C^{\nearrow}(k, l) = \frac{\sum_{i=1}^{U-2} \sum_{j=0}^{V-1} \delta(B(i+1, j) - k, B(i, j+1) - l)}{(U-1) \cdot (V-1)}, \quad (25)$$

where $k, l \in \{0, 1, \dots, 9\}$, and

$$\delta(m, n) = \begin{cases} 1, & m = n = 0, \\ 0, & \text{otherwise.} \end{cases} \quad (26)$$

Since we get six TLBP images (one for $R = 1$, two for $R = 2$, and three for $R = 3$) from each residual image, we will have a total number of $16 \times 6 \times 4 = 384$ co-occurrence matrices for all TLBP images from linear residual images, and $12 \times 6 \times 4 = 288$ co-occurrence matrices for all TLBP images from non-linear residual images.

B. Feature Aggregation

In order to reduce feature dimension, elements in co-occurrence matrices are aggregated in three ways.

Firstly, co-occurrence matrices along horizontal and vertical directions are merged, and those along diagonal and

anti-diagonal directions are merged as follows:

$$C^+(k, l) = C^{\downarrow}(k, l) + C^{\nwarrow}(k, l), \quad (27)$$

$$C^{\times}(k, l) = C^{\nearrow}(k, l) + C^{\swarrow}(k, l). \quad (28)$$

This will reduce the number of co-occurrence matrices to $16 \times 6 \times 2 = 192$ for all linear residual images, and $12 \times 6 \times 2 = 144$ for all non-linear residual images.

Secondly, co-occurrence matrixes obtained from $R_{\tilde{D}(0^\circ)}$ are merged with those from $R_{\tilde{D}(90^\circ)}$, where \tilde{D} is in the filter class from C#1 to C#3, as shown in Table I. This will reduce the number of co-occurrence matrices to $(\frac{12}{2} + 4) \times 6 \times 2 = 120$ for TLBP images from linear residual images.

Thirdly, non-diagonal elements in a co-occurrence matrix are merged with their counterparts from a transposed version of the matrix. The resultant combined elements and the diagonal elements are reshaped as a vector, i.e.,

$$c\left(9k - \frac{k(k-1)}{2} + l\right) = \begin{cases} C(k, l), & k = l, \\ C(k, l) + C(l, k), & k < l. \end{cases} \quad (29)$$

Such a process will result in 55-dimensional (55-D) merged features for each co-occurrence matrix. As a result, for unquantized residual images, we will get $(120 + 144) \times 55 = 14520$ features. When both quantized and unquantized residual images are used, we get a total feature dimension of 29040.

Note that the feature aggregation is similar to the co-occurrence symmetrization in SRM. However, since the proposed scheme computes co-occurrence from TLBP images

which do not have signs, sign symmetrical merging used in SRM is not applicable. Besides, we do not merge co-occurrence from “max” and “min” residuals.

C. Non-Linear Mapping

We note that the dynamic range of non-zero elements of the aggregated features is large. For instance, the range is from 10^{-6} (*i.e.*, $\frac{1}{(U-1) \times V}$ when $U = V = 512$) to 10^{-1} . This is due to the nature of co-occurrence matrix in which the diagonal elements are often large, while off-diagonal elements are often small. Large feature values might dominate the classification performance. In order to increase the efficiency of small features, we take the logarithm of features:

$$c' = \log(c + \delta), \quad (30)$$

where c is the feature value, and δ is a small constant (*e.g.*, $\frac{1}{(U-1) \times V}$) to prevent errors when $c = 0$. Such a non-linear mapping operation reduces the dynamic range and maintains monotonicity.

We note that feature transforms are studied in [38] and [39] to boost feature performance. In contrast to the methods in [38] and [39] which require a set of training images for parameter training and the method in [38] requires learning the parameters separately for each feature sub-model, the proposed non-linear mapping operation is simple and does not need training. Besides, the method in [38] approximates kernel tricks and may be generalizable to other features, while the logarithm mapping is an integrate part of the proposed feature extraction process for reducing the dynamic range and may only be adapted to the proposed features.

VI. EXPERIMENTS

A. Experimental Setup

In order to evaluate the performance of the proposed method, two kinds of tests are performed. Their settings are as follows.

1) *Performance Test*: In the performance test, we aim to find out how well a steganalytic method performs in detecting a specific steganographic scheme. It is straightforward that the lower the detection error, the better the steganalytic performance. In such a test, we randomly select a half number of the cover and the corresponding stego image pairs from a dataset for training, while use the rest image pairs for testing. With ten times of training/testing random splits, the steganalytic performance is evaluated by the averaged testing error, denoted as \bar{P}_E , as did in [5]. Most of the experiments in this section are performed in this way as default.

2) *Statistical Significance Test*: In the statistical significance test, we aim to find out whether two kinds of steganalytic methods, say \underline{A} and \underline{B} , have significant performance difference in the statistical sense. We adopt a statistical hypothesis testing method called *5 × 2 fold cross-validated pair t-test* [40], abbreviated as *t-test* hereafter. Suppose there are two hypothesis, the null and the alternative. The null hypothesis is that there is no significant difference in performance between \underline{A} and \underline{B} . The alternative hypothesis is that the performance differs.

A statistic \tilde{t} following the *Student's t distribution* is constructed, and a significance level α is selected to determine a threshold t_α ($t_\alpha > 0$). If $\tilde{t} > t_\alpha$, reject the null hypothesis and accept the alternative hypothesis, which means \underline{A} statistically performs better than \underline{B} . If $\tilde{t} < -t_\alpha < 0$, the relation between \underline{A} and \underline{B} is inverse, which means \underline{B} statistically performs better than \underline{A} . Otherwise, accept the null hypothesis. In the test, five replications of twofold cross-validation are performed. In each replication, all image pairs are randomly divided into two equal-size sets, S_1 and S_2 . Two methods are trained on each set and tested on the other set. Denote $p_A^{(1)}(i)$ and $p_B^{(1)}(i)$ the testing error of method \underline{A} and that of \underline{B} , respectively, in the i -th replication when the classifier is trained on S_1 and tested on S_2 . Similarly, denote $p_A^{(2)}(i)$ and $p_B^{(2)}(i)$ the testing errors for training on S_2 and testing on S_1 , respectively. Following [40] and after some simple arithmetic operations, a statistic \tilde{t} is constructed as

$$\tilde{t} = \frac{p_A^{(1)}(1) - p_B^{(1)}(1)}{s}, \quad (31)$$

where

$$s = \sqrt{\frac{1}{10} \sum_{i=1}^5 (p_A^{(1)}(i) - p_B^{(1)}(i) + p_B^{(2)}(i) - p_A^{(2)}(i))^2}. \quad (32)$$

When a significant level $\alpha = 0.95$ is selected, we get $t_\alpha = 2.015$. Unless mentioned otherwise, our experiments are carried out on BOSSBase 1.01 [37], which contains 10000 gray-scale cover images of dimension 512×512 . Fisher linear discriminant (FLD) based ensemble classifier [13] is applied for classification.

B. Performance of Each Feature Subset

TLBP features can be grouped into several parts according to their origin attributes, such as filter classes, residual types, quantization operations, and neighboring pixel sets. We investigate the effectiveness of each part by using four content-adaptive steganographic schemes, including S-UNIWARD [3], HILL [41], MiPOD [4], and CMD-HILL [5], with the payload rate of 0.4 bit per pixel (bpp). The dimensionality of each feature subset and the evaluation results are demonstrated in Table IV.

1) *Filter Class*: TLBP features can be divided into four subsets based on their origins being from filter class $C\#1$ to $C\#4$. From Table IV, we observe that features from $C\#3$ and $C\#4$ always perform better than those from $C\#1$ and $C\#2$. The reason may be due to the fact that more pixels are involved in the filtering operations in $C\#3$ and $C\#4$.

2) *Residual Type*: TLBP features can be divided into two subsets according to their origins being from linear residuals or from non-linear residuals. From Table IV, we can conclude that features generated from non-linear residuals perform slightly better than those from linear residuals.

3) *Quantization Operation*: According to whether the residuals are quantized or not, TLBP features can be divided into two subsets. Table IV shows that features generated from quantized residuals perform far better than those from unquantized residuals. Even so, combining features from quantized and

TABLE IV
DETECTION PERFORMANCE (\bar{P}_E) FOR DIFFERENT SETS OF FEATURES

Grouping Criterion	Feature Subset	Feature Dimension	S-UNIWARD	HILL	MiPOD	CMD-HILL
Filter Class	$C\#1$	7,920-D	0.2276	0.2960	0.2908	0.3366
	$C\#2$	7,920-D	0.2302	0.2865	0.2827	0.3321
	$C\#3$	7,920-D	0.2121	0.2362	0.2357	0.3039
	$C\#4$	5,280-D	0.2254	0.2483	0.2460	0.3148
Residual Type	Linear	13,200-D	0.2020	0.2415	0.2373	0.3006
	Nonlinear	15,840-D	<u>0.1974</u>	<u>0.2379</u>	<u>0.2364</u>	<u>0.2976</u>
Quantization Operation	Quantized-and-Truncated	14,520-D	0.2067	0.2320	0.2301	0.2940
	Unquantized	14,520-D	0.2076	0.2623	0.2584	0.3180
Neighboring Pixel Set	$R = 1$	4,840-D	0.2270	0.2782	0.2760	0.3333
	$R = 2, \text{subset}\#1$	4,840-D	0.2220	0.2640	0.2611	0.3272
	$R = 2, \text{subset}\#2$	4,840-D	0.2086	0.2461	0.2449	0.3084
	$R = 3, \text{subset}\#1$	4,840-D	0.2378	0.2788	0.2795	0.3360
	$R = 3, \text{subset}\#2$	4,840-D	0.2216	0.2531	0.2547	0.3171
	$R = 3, \text{subset}\#3$	4,840-D	0.2206	0.2580	0.2567	0.3199

TABLE V

COMPARISON ON THE DETECTION PERFORMANCE (\bar{P}_E) FOR DIFFERENT STEGANOGRAPHIC SCHEMES. THE RESULT IS UNDERLINED WHEN TLBP PERFORMS BETTER THAN SRM AND LBP-HIST, AND IT IS MARKED WITH BOLD FONT WHEN TLBP PERFORMS BETTER THAN MAXSRM

Steganographic Scheme	Steganalytic Feature	0.1 bpp	0.2 bpp	0.3 bpp	0.4 bpp	0.5 bpp
S-UNIWARD	TLBP	0.4062	<u>0.3212</u>	<u>0.2494</u>	0.1893	0.1447
	SRM	0.4006	<u>0.3227</u>	<u>0.2547</u>	0.2074	0.1629
	LBP-HIST	0.4253	0.3500	0.2898	0.2299	0.1921
	maxSRM	0.3699	0.2986	0.2428	0.1975	0.1627
HILL	TLBP	0.4106	<u>0.3399</u>	<u>0.2791</u>	<u>0.2295</u>	0.1888
	SRM	<u>0.4340</u>	<u>0.3621</u>	<u>0.2975</u>	<u>0.2483</u>	0.2035
	LBP-HIST	0.4532	0.3923	0.3336	0.2807	0.2343
	maxSRM	0.3790	0.3174	0.2679	0.2244	0.1890
MiPOD	TLBP	0.4075	<u>0.3361</u>	0.2768	0.2271	0.1872
	SRM	<u>0.4162</u>	<u>0.3432</u>	<u>0.2858</u>	<u>0.2374</u>	0.2003
	LBP-HIST	0.4360	0.3743	0.3197	0.2690	0.2274
	maxSRM	0.4030	0.3318	0.2786	0.2315	0.1957
CMD-HILL	TLBP	<u>0.4408</u>	<u>0.3838</u>	<u>0.3350</u>	<u>0.2881</u>	<u>0.2489</u>
	SRM	0.4529	0.3945	0.3424	0.2987	0.2542
	LBP-HIST	0.4699	0.4240	0.3758	0.3332	0.2921
	maxSRM	0.4019	0.3495	0.3037	0.2698	0.2356

unquantized subsets can increase feature diversity and boost performance, as shown in the results in the next subsection.

4) *Neighboring Pixel Set*: As illustrated in Fig. 3, six neighboring pixel sets are used in TLBP scheme, and, correspondingly, TLBP features can be divided into six subsets. It can be observed from Table IV that the features from $R = 2$ (subset#2) perform the best.

From the results shown in Table IV, we can observe that the best feature subset is stable across different steganographic schemes. It indicates that whenever high dimensionality is a problem, we can achieve a trade-off between dimensionality and performance by using a subset of features.

C. Comparison With Prior Arts

We use two most related steganalytic feature sets, namely SRM [19] with 34671-D features and LBP-HIST [25] with 22153-D features, for comparison. A special kind of steganalytic feature set, maxSRM [21] with 34671-D features, which incorporates probabilistic selection channel information into SRM, is also included as a reference. Four content-adaptive steganographic schemes, as used in the previous sub-section, are employed for evaluation. The payload rate is set from 0.1 to 0.5 bpp.

We show the results of performance test in Table V. It can be observed that, except for the case on S-UNIWARD with a small payload where TLBP performs slightly poorer than SRM, the proposed TLBP scheme always achieves lower detection error than SRM and LBP-HIST. The maxSRM scheme often achieves the best performance for low payload rates and always performs best on CMD-HILL. This is not surprised because it incorporates the knowledge of embedding change probabilities, and when the payload rate is low, the change probabilities are highly nonuniform and provide more useful information in detection. When the payload rate is high for S-UNIWARD, HILL, and MiPOD, the advantage in maxSRM is not prominent.

We show the results of statistical significance test in Table VI for comparing TLBP with SRM and maxSRM, respectively. The results indicate that TLBP performs statistically better than SRM in most cases. When comparing TLBP with maxSRM, it is hard to say whether TLBP is better or worse than maxSRM in the statistical sense for 40% (8 out of 20) of the cases. However, when used for detecting CMD-HILL, maxSRM always performs better, which indicates the knowledge of selection channel leads to benefits.

TABLE VI

THE VALUE OF THE STATISTIC \tilde{t} IN T-TEST. THE VALUES ARE BOXED WHEN TLBP PERFORMS STATISTICALLY SIGNIFICANT BETTER, AND UNDERLINED WHEN TLBP PERFORMS STATISTICALLY SIGNIFICANT WORSE. THE VALUES WITH PLAIN STYLE INDICATE THE NULL HYPOTHESIS IS ACCEPTED (WITH SIGNIFICANCE LEVEL $\alpha = 0.95$)

Comparison Schemes	Steganographic Scheme	0.1 bpp	0.2 bpp	0.3 bpp	0.4 bpp	0.5 bpp
TLBP vs SRM	S-UNIWARD	-0.779	0.274	2.278	3.707	7.032
	HILL	<u>6.251</u>	<u>3.238</u>	2.206	4.221	4.862
	MiPOD	0.741	<u>2.838</u>	4.001	4.276	4.561
	CMD-HILL	1.863	<u>2.432</u>	3.128	2.812	1.474
TLBP vs maxSRM	S-UNIWARD	<u>-7.247</u>	<u>-5.798</u>	-1.708	0.170	3.132
	HILL	<u>-9.291</u>	<u>-3.154</u>	-0.423	-0.720	1.184
	MiPOD	-0.804	-0.508	<u>3.496</u>	1.795	<u>2.167</u>
	CMD-HILL	<u>-7.811</u>	<u>-6.858</u>	<u>-4.857</u>	<u>-8.328</u>	<u>-4.677</u>

TABLE VII

THE DIMENSION OF THE SELECTED SUB-FEATURES AND THE RATIO OF THE SELECTED SUB-FEATURES OVER THE COMPLETE FEATURE SET (SHOWN IN BOLD FONT)

Steganographic Scheme	Steganalytic Feature	0.1 bpp	0.2 bpp	0.3 bpp	0.4 bpp	0.5 bpp
S-UNIWARD	TLBP	1420 0.05	1620 0.06	1660 0.06	1880 0.06	1780 0.06
	SRM	1460 0.04	1500 0.04	1640 0.05	1420 0.04	1680 0.05
	LBP-HIST	1320 0.06	1520 0.07	1280 0.06	1360 0.06	1620 0.07
	maxSRM	1020 0.03	1340 0.04	1350 0.04	1270 0.04	1350 0.04
HILL	TLBP	1340 0.05	1500 0.05	1420 0.05	1620 0.06	1640 0.06
	SRM	1080 0.03	1620 0.05	1900 0.05	1680 0.05	1660 0.05
	LBP-HIST	860 0.04	1080 0.05	1260 0.06	1390 0.06	1480 0.07
	maxSRM	1020 0.03	1020 0.03	1240 0.04	1100 0.03	1240 0.04
MiPOD	TLBP	1360 0.05	1420 0.05	1680 0.06	1560 0.05	1680 0.06
	SRM	1460 0.04	1720 0.05	1720 0.05	1540 0.04	1620 0.05
	LBP-HIST	1180 0.05	1180 0.05	1220 0.06	1420 0.06	1380 0.06
	maxSRM	960 0.03	960 0.03	1080 0.03	1180 0.03	1140 0.03
CMD-HILL	TLBP	1180 0.04	1340 0.05	1480 0.05	1540 0.05	1700 0.06
	SRM	900 0.03	1900 0.05	1640 0.05	1580 0.05	1720 0.05
	LBP-HIST	880 0.04	1160 0.05	1320 0.06	1440 0.07	1300 0.06
	maxSRM	1040 0.03	1160 0.03	1180 0.03	1020 0.03	1260 0.04

Note that the comparison between TLBP/SRM/LBP-HIST and maxSRM is in different cases. The knowledge of selection channel is not assumed in the first three schemes, which may be a more common case in steganographic scenarios. It is tempting to incorporate the selection channel information in TLBP to detect content-adaptive steganographic schemes.

D. Investigation on Feature Utilization and Efficiency

Since the feature dimension is different among SRM/maxSRM, LBP-HIST, and TLBP, we would like to investigate the feature utilization and efficiency. Firstly, we investigate how many features are employed in the ensemble

classifier [13]. The ensemble classifier is equipped with several linear base learners, and each base learner performs classification in a sub-space by randomly sub-sampling features from the whole feature space. The optimal amount of the sub-learners (denoted as d_L) and the optimal number of the sub-features (denoted as d_{sub}) are found by exhaustive search to optimize the training performance. Table VII shows d_{sub} and d_{sub}/d (where d is number of the complete feature set), and Table VIII shows d_L used in the ensemble classifier, respectively. We can observe that as the payload rate increases, the dimension of selected sub-features generally increases for all steganalytic features. However, the trends are not always

TABLE VIII
THE NUMBER OF BASE LEARNERS USED BY ENSEMBLE CLASSIFIER IN DETECTING STEGANOGRAPHY

Steganographic Scheme	Steganalytic Feature	0.1 bpp	0.2 bpp	0.3 bpp	0.4 bpp	0.5 bpp
S-UNIWARD	TLBP	95	112	110	110	101
	SRM	76	98	111	94	109
	LBP-HIST	107	99	113	114	107
	maxSRM	126	115	120	108	114
HILL	TLBP	95	100	100	98	96
	SRM	74	88	113	99	97
	LBP-HIST	95	108	102	114	106
	maxSRM	121	107	113	107	105
MiPOD	TLBP	103	98	108	101	99
	SRM	80	102	105	103	94
	LBP-HIST	107	99	113	114	105
	maxSRM	118	109	117	110	103
CMD-HILL	TLBP	100	103	107	114	108
	SRM	76	99	103	101	102
	LBP-HIST	96	97	109	109	107
	maxSRM	117	131	129	119	110

TABLE IX
DETECTION PERFORMANCE (\bar{P}_E) WHEN FEATURE MAPPING IS USED

Steganographic Scheme	Steganalytic Feature	0.1 bpp	0.2 bpp	0.3 bpp	0.4 bpp	0.5 bpp
S-UNIWARD	SRM (log mapping)	0.3998	0.3250	0.2625	0.2092	0.1626
	SRM (exp-Hellinger mapping)	0.3918	0.3075	0.2396	0.1856	0.1413
	maxSRM (log mapping)	0.3805	0.2977	0.2365	0.1897	0.1493
	maxSRM (exp-Hellinger mapping)	0.3664	0.2845	0.2256	0.1778	0.1385
	LBP-HIST (log mapping)	0.4240	0.3489	0.2861	0.2317	0.1872
	TLBP (exp-Hellinger mapping, 660-D)	0.4108	0.3305	0.2579	0.1991	0.1510
	TLBP (exp-Hellinger mapping, 330-D)	0.4093	0.3285	0.2594	0.1997	0.1544
HILL	SRM (log mapping)	0.4132	0.3524	0.2963	0.2525	0.2113
	SRM (exp-Hellinger mapping)	0.4064	0.3387	0.2785	0.2292	0.1856
	maxSRM (log mapping)	0.3808	0.3126	0.2601	0.2189	0.1839
	maxSRM (exp-Hellinger mapping)	0.3696	0.3005	0.2493	0.2052	0.1680
	LBP-HIST (log mapping)	0.4448	0.3803	0.3201	0.2719	0.2270
	TLBP (exp-Hellinger mapping, 660-D)	0.4208	0.3507	0.2915	0.2417	0.2005
	TLBP (exp-Hellinger mapping, 330-D)	0.4185	0.3498	0.2900	0.2425	0.2002
MiPOD	SRM (log mapping)	0.4102	0.3446	0.2904	0.2451	0.2080
	SRM (exp-Hellinger mapping)	0.4024	0.3299	0.2699	0.2225	0.1828
	maxSRM (log mapping)	0.4027	0.3294	0.2706	0.2261	0.1891
	maxSRM (exp-Hellinger mapping)	0.3938	0.3213	0.2631	0.2142	0.1771
	LBP-HIST (log mapping)	0.4342	0.3666	0.3135	0.2647	0.2222
	TLBP (exp-Hellinger mapping, 660-D)	0.4142	0.3456	0.2876	0.2413	0.1978
	TLBP (exp-Hellinger mapping, 330-D)	0.4128	0.3483	0.2876	0.2392	0.1981
CMD-HILL	SRM (log mapping)	0.4357	0.3816	0.3358	0.2940	0.2560
	SRM (exp-Hellinger mapping)	0.4312	0.3712	0.3188	0.2755	0.2359
	maxSRM (log mapping)	0.4018	0.3447	0.3004	0.2610	0.2273
	maxSRM (exp-Hellinger mapping)	0.3911	0.3361	0.2884	0.2496	0.2162
	LBP-HIST (log mapping)	0.4656	0.4144	0.3675	0.3259	0.2828
	TLBP (exp-Hellinger mapping, 660-D)	0.4495	0.3946	0.3509	0.3015	0.2622
	TLBP (exp-Hellinger mapping, 330-D)	0.4500	0.3954	0.3495	0.3027	0.2644

monotonic. It is interesting to see that maxSRM always uses less sub-features (around 3% to 4% of the complete feature set) compared to SRM (around 4% to 5% of the complete feature set). However, it uses typically more base learners (around 105 to 120) than SRM (around 80 to 110). LBP-HIST uses 4% to 7% of the features, and uses around 95 to 114 base learners, while TLBP typically uses 5% to 6% of the features, and uses around 100 to 110 base learners. As reported in [42], the training time of ensemble classifier is related to the number of selected sub-features and base learners. Since the dimensions of sub-features used in the four schemes do not

have great difference, the differences in training time are ignorable.

Secondly, we use Laplacian Score [32], a kind of feature selection method relies on Laplacian eigen-maps and locality preserving projection, to evaluate feature efficiency. It is carried out in a supervised manner in the experiments. The higher the score is, the more effective the individual feature. Hence, we sort features in each feature set according to the scores in a descending order, and select the features with highest scores to perform steganalysis. The results are shown in Fig. 5. We can observe that under the same number

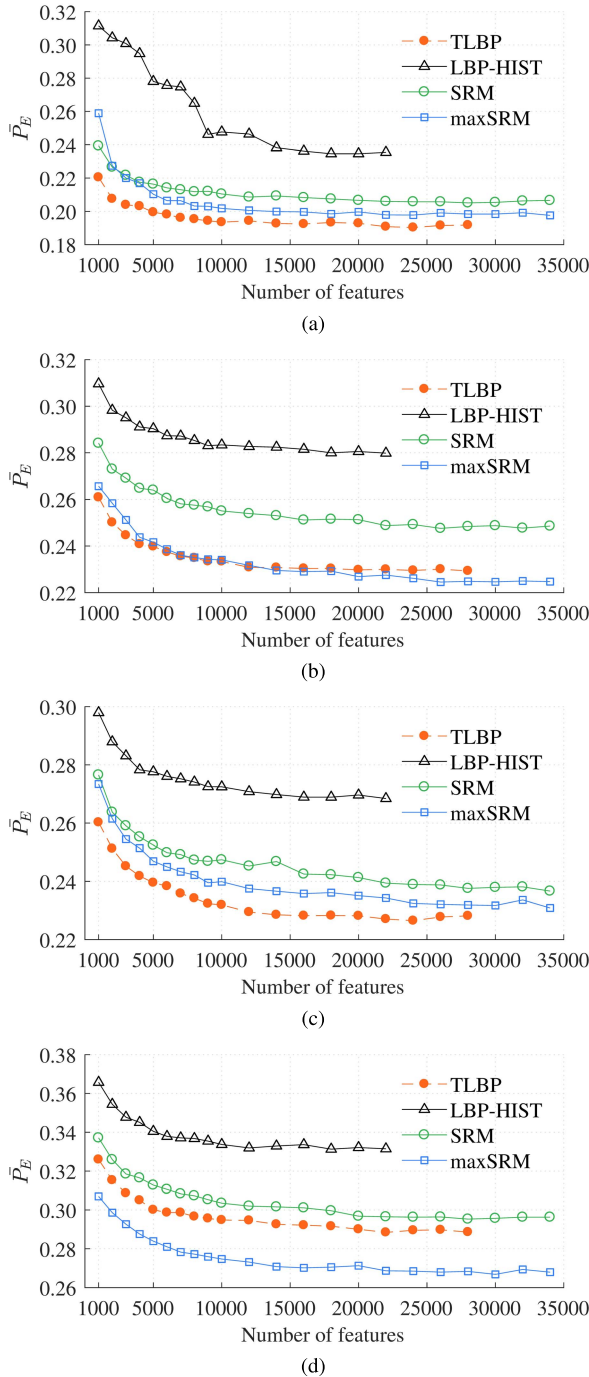


Fig. 5. Detection performance of TLBP, LBP-HIST, SRM, and maxSRM on detecting each steganography with selected features according to Laplacian Score. (a) S-UNIWARD 0.4 bpp. (b) HILL 0.4 bpp. (c) MiPOD 0.4 bpp. (d) CMD-HILL 0.4 bpp

of features, TLBP consistently performs the best to detect S-UNIWARD and MiPOD under the payload rate of 0.4 bpp.

E. Performance With Non-Linear Feature Mapping

In [38] and [39], explicit non-linear transformations of features are studied to boost the steganalytic ability. These methods may not be limited to boost SRM/maxSRM, but require training images for parameter setting. The method in [38] also requires learning the parameters separately for each feature

sub-model. On the contrary, the logarithm mapping integrated in the proposed TLBP feature extraction process is simple to reduce the high dynamic ranges of arbitrary features without training, but it is not designed to be generalizable for other features.

To investigate the effect of feature mapping, we perform experiments as follows. On one hand, we perform the logarithm mapping as (30) on SRM, maxSRM, and LBP-HIST, respectively. On the other hand, we perform the exponential-Hellinger kernel mapping, which obtained the best results in [38], on SRM, maxSRM, and TLBP. In this case, we use two kinds of feature sub-models for TLBP, with the dimension 660-D and 330-D, respectively. For the 660-D sub-models, we use features from all six TLBP images from a residual image, as illustrated in the dashed box in Fig. 4. In order to be easily compared with the SRM sub-models with 325-D/338-D, the 330-D sub-models are obtained from the 660-D sub-models, by dividing them into two parts where features of three LBP images from $R = 1$ and $R = 2$ (referred to Fig. 3) form a part, and those from $R = 3$ form another. It is difficult to construct sub-models for LBP-HIST, and therefore the corresponding performance with exponential-Hellinger mapping is not reported. A number of 350 images are used for training the mapping parameter for SRM, maxSRM, and TLBP (330-D), and a number of 660 images are used for training TLBP (660-D). Since the method in [39] for SRM/maxSRM has similar performance with that in [38], and it is not directly applicable to TLBP and LBP-HIST, we do not include it for comparison.

Table IX shows the results. By comparing them with Table V, it can be observed that the maxSRM features processed with the exponential-Hellinger kernel mapping achieve the best performance, while the SRM features with the exponential-Hellinger kernel mapping have close performance with TLBP. It can also be observed that the logarithm mapping does not work well on SRM and maxSRM. Similarly, the exponential-Hellinger kernel mapping does not work well on TLBP. LBP-HIST equipped with logarithm mapping has a slight but not distinct improvement. We may conclude that non-linear mapping plays an important role in boosting feature effectiveness. However, it should be adapted to each feature set by considering its characteristics.

F. Performance Under Different Training Sizes

Since high-dimensional features are used in steganalysis, the number of training samples may have an impact to performance. We perform experiments by gradually increasing the number of training image pairs, from 3000 to 8000 with a step of 1000, and use the rest image pairs in BOSSBase for testing. The results for the four steganographic schemes with the payload rate of 0.4 bpp and 0.2 bpp are shown in Table X. We can conclude that with the increasing number of training images, all steganalytic features perform better.

G. Performance on A Combined Dataset

In order to investigate the performance of TLBP on a larger dataset, we have performed an experiment on a combined dataset with 18000 cover images, where a cover dataset,

TABLE X
PERFORMANCE WITH DIFFERENT NUMBER OF TRAINING IMAGE PAIRS ON BOSSBASE DATASET

Steganographic Scheme	Steganalytic Feature	3,000	4,000	5,000	6,000	7,000	8,000
S-UNIWARD (0.4 bpp)	TLPB	0.1995	0.1923	0.1887	0.1866	0.1834	0.1826
	SRM	0.2125	0.2076	0.2058	0.2035	0.2009	0.2003
	maxSRM	0.2083	0.2019	0.1975	0.1962	0.1936	0.1930
S-UNIWARD (0.2 bpp)	TLPB	0.3299	0.3267	0.3208	0.3203	0.3170	0.3161
	SRM	0.3257	0.3231	0.3196	0.3202	0.3164	0.3185
	maxSRM	0.3058	0.3012	0.2986	0.2931	0.2920	0.2895
HILL (0.4 bpp)	TLPB	0.2373	0.2337	0.2305	0.2273	0.2249	0.2231
	SRM	0.2522	0.2493	0.2467	0.2448	0.2433	0.2437
	maxSRM	0.2321	0.2269	0.2244	0.2223	0.2202	0.2201
HILL (0.2 bpp)	TLPB	0.3454	0.3448	0.3410	0.3359	0.3366	0.3337
	SRM	0.3490	0.3453	0.3427	0.3421	0.3412	0.3403
	maxSRM	0.3237	0.3194	0.3174	0.3146	0.3120	0.3103
MiPOD (0.4 bpp)	TLPB	0.2348	0.2307	0.2276	0.2253	0.2243	0.2212
	SRM	0.2448	0.2398	0.2369	0.2344	0.2333	0.2315
	maxSRM	0.2389	0.2349	0.2315	0.2312	0.2274	0.2266
MiPOD (0.2 bpp)	TLPB	0.3415	0.3397	0.3369	0.3342	0.3322	0.3320
	SRM	0.3470	0.3462	0.3443	0.3421	0.3404	0.3414
	maxSRM	0.3341	0.3281	0.3318	0.3266	0.3257	0.3260
CMD-HILL (0.4 bpp)	TLPB	0.2968	0.2927	0.2908	0.2886	0.2856	0.2834
	SRM	0.3016	0.2995	0.2962	0.2952	0.2927	0.2906
	maxSRM	0.2751	0.2712	0.2716	0.2657	0.2649	0.2621
CMD-HILL (0.2 bpp)	TLPB	0.3879	0.3855	0.3848	0.3821	0.3810	0.3799
	SRM	0.3974	0.3959	0.3951	0.3954	0.3916	0.3906
	maxSRM	0.3535	0.3507	0.3687	0.3464	0.3464	0.3431

TABLE XI
PERFORMANCE WITH DIFFERENT NUMBER OF TRAINING IMAGE PAIRS ON COMBINED DATASET

Steganographic Scheme	Steganalytic Feature	5,000	7,000	9,000	11,000	13,000	15,000
S-UNIWARD (0.4 bpp)	TLPB	0.2253	0.2199	0.2142	0.2131	0.2079	0.2006
	SRM	0.2423	0.2373	0.2390	0.2370	0.2265	0.2222
	maxSRM	0.2275	0.2212	0.2173	0.2128	0.2096	0.2080
S-UNIWARD (0.2 bpp)	TLPB	0.3481	0.3429	0.3422	0.3344	0.3325	0.3277
	SRM	0.3504	0.3489	0.3443	0.3434	0.3392	0.3350
	maxSRM	0.3179	0.3117	0.3053	0.3066	0.3020	0.3003
HILL (0.4 bpp)	TLPB	0.2541	0.251	0.2522	0.2430	0.2408	0.2360
	SRM	0.2855	0.2809	0.2754	0.2810	0.2726	0.2705
	maxSRM	0.2447	0.2404	0.2443	0.2380	0.2348	0.2303
HILL (0.2 bpp)	TLPB	0.3569	0.3521	0.3536	0.3476	0.3426	0.3389
	SRM	0.3868	0.3842	0.3821	0.3790	0.3780	0.3773
	maxSRM	0.3282	0.3244	0.3226	0.3210	0.3164	0.3132
MiPOD (0.4 bpp)	TLPB	0.2539	0.2483	0.2521	0.2422	0.2392	0.2355
	SRM	0.2759	0.2703	0.2726	0.2738	0.2625	0.2570
	maxSRM	0.2565	0.2526	0.2522	0.2492	0.2433	0.2395
MiPOD (0.2 bpp)	TLPB	0.3573	0.3523	0.3506	0.3534	0.3458	0.3411
	SRM	0.3739	0.3718	0.3696	0.3712	0.3652	0.3645
	maxSRM	0.3510	0.3475	0.3446	0.3430	0.3391	0.3369
CMD-HILL (0.4 bpp)	TLPB	0.3196	0.315	0.3175	0.3141	0.3048	0.3014
	SRM	0.2759	0.336	0.3370	0.3344	0.3277	0.3253
	maxSRM	0.302	0.2979	0.2945	0.2931	0.2904	0.2857
CMD-HILL (0.2 bpp)	TLPB	0.403	0.3981	0.3971	0.3942	0.3906	0.3902
	SRM	0.4229	0.4226	0.4184	0.4284	0.4174	0.4161
	maxSRM	0.3711	0.3689	0.3670	0.3640	0.3625	0.3594

MRNC (Mixed Resized Never-Compressed),¹ is combined with BOSSBase. MRNC contains 8000 gray-scale images of size 768×768 and was used in [5] to evaluate steganographic schemes. We use 5000 to 15000 (with a step of 2000) cover and stego image pairs for training, and use the rest 13000 to 3000 pairs for testing. In the combined training set, the number

of image pairs selected from BOSSBase is 1000 more than that from MRNC. The results are shown in Table XI. It can be observed that even though we use more images for training, the performances of all steganalytic methods are worse on this combined dataset than those on BOSSBase. This may be due to a mixture of different image sources, where the origin, the size, and the down-sampling method are different. The relative relation in performance among TLPB, SRM, and maxSRM on the combined dataset is similar to that on BOSSBase.

¹It can be downloaded from <http://media-sec.szu.edu.cn/couch/uploads/file/MRNC.rar>

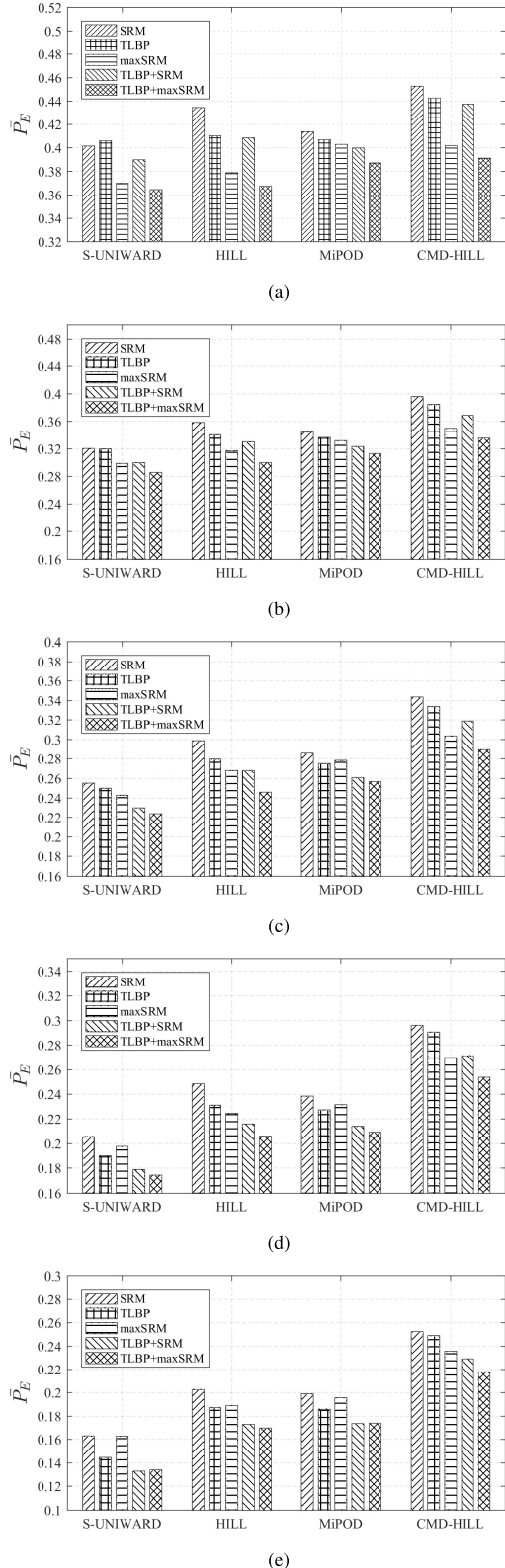


Fig. 6. Detection performance of TLBP, SRM, maxSRM, the combination of TLBP and SRM, and the combination of TLBP and maxSRM. (a) Payload 0.1 bpp. (b) Payload 0.2 bpp. (c) Payload 0.3 bpp. (d) Payload 0.4 bpp. (e) Payload 0.5 bpp.

H. Performance of Combined Feature Set

The proposed TLBP features are designed in a different way from SRM/maxSRM features. Specifically, TLBP operation is

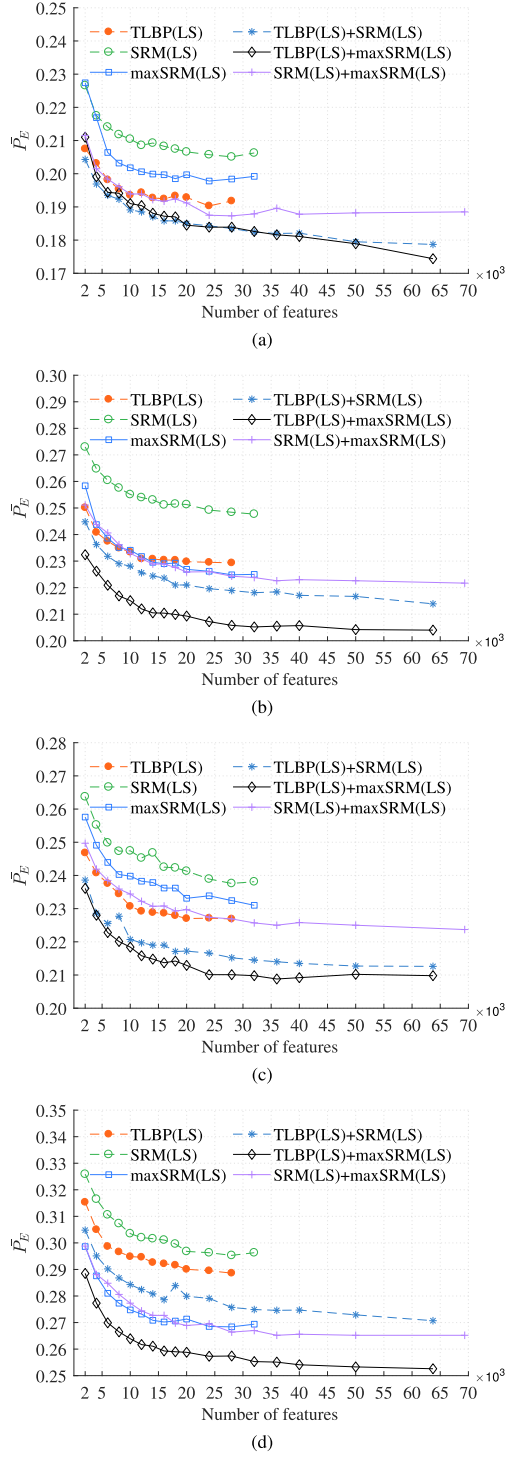


Fig. 7. Performance of TLBP, SRM, maxSRM, and the combinations of them on detecting different steganographic schemes by using selected features with the highest Laplacian Score values. (a) S-UNIWARD 0.4 bpp. (b) HILL 0.4 bpp. (c) MiPOD 0.4 bpp. (d) CMD-HILL 0.4 bpp.

introduced before using co-occurrence matrix to characterize pixel relationship in a larger extent. Since TLBP/LBP operation is very different from co-occurrence matrix in describing local features, they may be complementary to each other. As shown in Fig. 6, when combining TLBP with SRM, and combining TLBP with maxSRM, respectively, to form features with 63711-D, better performance can be expected. It can be

observed that TLBP combined with SRM performs better than maxSRM when the payload rate is high.

We show the complementarity between TLBP and SRM/maxSRM in another aspect. We perform experiments by combining the selected features with the top LS values, as did in Section VI-D. The combined feature set, denoted as TLBP(LS)+SRM(LS), TLBP(LS)+maxSRM(LS), and SRM(LS)+maxSRM(LS), is formed by an equal number of selected features from two different feature sets with the highest LS values. As demonstrated in Fig. 7, it is clear that the combined features are very effective under the same dimension when compared to the features only from the respective source. TLBP(LS)+maxSRM(LS) always achieves the best performance. It is interesting to observe that TLBP(LS)+SRM(LS) performs better than SRM(LS)+maxSRM(LS) on S-UNIWARD, HILL, and MiPOD, but performs worse on CMD-HILL. This may indicate that the knowledge of selection channel is more important when synchronous selection channel is presented.

VII. CONCLUSION

Steganalysis is a rather unique and difficult recognition task compared to many computer vision and image classification problems, due to its aim to discover imperceptible clues. In this paper, we propose a new steganalytic feature extraction scheme which consists of three major components. Firstly, a few high-order derivative filters are used to obtain a compact number of linear and non-linear residual images for evaluating intricate relationships among pixels. Secondly, a well-defined TLBP operator is proposed to further characterize the relation between image residuals. Because of its capability to characterize the magnitude relationship between the central element and its neighbors, it performs better than the standard LBP operator. Besides, the elements considered in TLBP can be selected from all directions, and it has better flexibility than directly using co-occurrences along a fixed direction. Thirdly, second-order co-occurrence matrix features are extracted to replace histogram features used in conventional LBP schemes. They have better modeling capability and low dimensionality as we processed them with aggregation and non-linear mapping.

The proposed TLBP features achieve good detection performance against several state-of-the-art content-adaptive steganographic methods under various conditions. When combined with the well-known SRM scheme, better performance can be obtained. In future work, we would like to investigate whether selection channel information can be incorporated in the TLBP scheme.

ACKNOWLEDGMENT

We appreciate Dr. Fuxiang Lu from Lanzhou University for introducing LBP and providing the code of [35]. We also appreciate the AE and the anonymous reviewers for their valuable comments.

REFERENCES

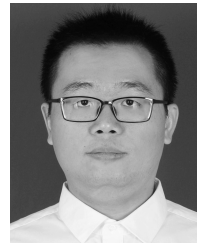
- [1] A. D. Ker *et al.*, “Moving steganography and steganalysis from the laboratory into the real world,” in *Proc. 1st ACM Workshop Inf. Hiding Multimedia Secur.*, 2013, pp. 45–58.
- [2] T. Pevný, T. Filler, and P. Bas, “Using high-dimensional image models to perform highly undetectable steganography,” in *Proc. Int. Workshop Inf. Hiding*, 2010, pp. 161–177.
- [3] V. Holub, J. Fridrich, and T. Denemark, “Universal distortion function for steganography in an arbitrary domain,” *EURASIP J. Inf. Secur.*, vol. 2014, no. 1, pp. 1–13, 2014.
- [4] V. Sedighi, R. Cogranne, and J. Fridrich, “Content-adaptive steganography by minimizing statistical detectability,” *IEEE Trans. Inf. Forensics Security*, vol. 11, no. 2, pp. 221–234, Feb. 2016.
- [5] B. Li, M. Wang, X. Li, S. Tan, and J. Huang, “A strategy of clustering modification directions in spatial image steganography,” *IEEE Trans. Inf. Forensics Security*, vol. 10, no. 9, pp. 1905–1917, Sep. 2015.
- [6] T. Denemark and J. Fridrich, “Improving steganographic security by synchronizing the selection channel,” in *Proc. 3rd ACM Workshop Inf. Hiding Multimedia Secur.*, 2015, pp. 5–14.
- [7] W. Zhou, W. Zhang, and N. Yu, “Evolving distortion function by exploiting the differences among comparable adaptive steganography,” in *Proc. IEEE 12th Int. Conf. Natural Comput., Fuzzy Syst. Knowl. Discovery*, Aug. 2016, pp. 2262–2271.
- [8] J. Fridrich and J. Kodovský, “Multivariate Gaussian model for designing additive distortion for steganography,” in *Proc. IEEE Int. Conf. Acoust., Speech Signal Process.*, May 2013, pp. 2949–2953.
- [9] K. Chen, W. Zhang, H. Zhou, N. Yu, and G. Feng, “Defining cost functions for adaptive steganography at the microscale,” in *Proc. IEEE Int. Workshop Inf. Forensics Secur.*, Dec. 2016, pp. 1–6.
- [10] T. Filler, J. Judas, and J. Fridrich, “Minimizing additive distortion in steganography using syndrome-trellis codes,” *IEEE Trans. Inf. Forensics Security*, vol. 6, no. 3, pp. 920–935, Sep. 2011.
- [11] X. Li, S. Cai, W. Zhang, and B. Yang, “A further study of large payloads matrix embedding,” *Inf. Sci.*, vol. 324, pp. 257–269, Dec. 2015.
- [12] W. Zhang, Z. Zhang, L. Zhang, H. Li, and N. Yu, “Decomposing joint distortion for adaptive steganography,” *IEEE Trans. Circuits Syst. Video Technol.*, vol. 27, no. 10, pp. 2274–2280, Oct. 2017.
- [13] J. Kodovský, J. Fridrich, and V. Holub, “Ensemble classifiers for steganalysis of digital media,” *IEEE Trans. Inf. Forensics Security*, vol. 7, no. 2, pp. 432–444, Apr. 2012.
- [14] R. Cogranne, V. Sedighi, J. Fridrich, and T. Pevný, “Is ensemble classifier needed for steganalysis in high-dimensional feature spaces?” in *Proc. IEEE Int. Workshop Inf. Forensics Secur.*, Nov. 2015, pp. 1–6.
- [15] S. Tan and B. Li, “Stacked convolutional auto-encoders for steganalysis of digital images,” in *Proc. IEEE Asia-Pacific Signal Inf. Process. Assoc. Annu. Summit Conf.*, Dec. 2014, pp. 1–4.
- [16] Y. Qian, J. Dong, W. Wang, and T. Tan, “Deep learning for steganalysis via convolutional neural networks,” *Proc. SPIE*, vol. 9409, p. 94090J, Mar. 2015.
- [17] G. Xu, H.-Z. Wu, and Y.-Q. Shi, “Structural design of convolutional neural networks for steganalysis,” *IEEE Signal Process. Lett.*, vol. 23, no. 5, pp. 708–712, May 2016.
- [18] J. Zeng, S. Tan, B. Li, and J. Huang, “Large-scale JPEG steganalysis using hybrid deep-learning framework,” *IEEE Trans. Inf. Forensics Security*, to be published, doi: [10.1109/TIFS.2017.2779446](https://doi.org/10.1109/TIFS.2017.2779446).
- [19] J. Fridrich and J. Kodovský, “Rich models for steganalysis of digital images,” *IEEE Trans. Inf. Forensics Security*, vol. 7, no. 3, pp. 868–882, Jun. 2012.
- [20] V. Holub and J. Fridrich, “Random projections of residuals for digital image steganalysis,” *IEEE Trans. Inf. Forensics Security*, vol. 8, no. 12, pp. 1996–2006, Dec. 2013.
- [21] T. Denemark, V. Sedighi, V. Holub, R. Cogranne, and J. Fridrich, “Selection-channel-aware rich model for steganalysis of digital images,” in *Proc. IEEE Int. Workshop Inf. Forensics Secur.*, Dec. 2014, pp. 48–53.
- [22] W. Tang, H. Li, W. Luo, and J. Huang, “Adaptive steganalysis based on embedding probabilities of pixels,” *IEEE Trans. Inf. Forensics Security*, vol. 11, no. 4, pp. 734–745, Apr. 2016.
- [23] J. Kodovský and J. Fridrich, “Steganalysis of JPEG images using rich models,” *Proc. SPIE*, vol. 8303, p. 83030A, Feb. 2012.
- [24] M. Goljan, J. Fridrich, and R. Cogranne, “Rich model for steganalysis of color images,” in *Proc. IEEE Int. Workshop Inf. Forensics Secur.*, Dec. 2014, pp. 185–190.
- [25] Y. Q. Shi, P. Sutthiwat, and L. Chen, “Textural features for steganalysis,” in *Proc. Int. Workshop Inf. Hiding*, 2012, pp. 63–77.
- [26] B. Li, J. Huang, and Y. Q. Shi, “Textural features based universal steganalysis,” *Proc. SPIE*, vol. 6819, p. 681912, Mar. 2008.
- [27] P. Lafferty and F. Ahmed, “Texture-based steganalysis: Results for color images,” *Proc. SPIE*, vol. 5561, pp. 145–151, Oct. 2004.

- [28] X. Gui, X. Li, and B. Yang, "Steganalysis of LSB matching based on local binary patterns," in *Proc. IEEE 10th Int. Conf. Intell. Inf. Hiding Multimedia Signal Process.*, Aug. 2014, pp. 475–480.
- [29] T. Ojala, M. Pietikäinen, and D. Harwood, "A comparative study of texture measures with classification based on feature distributions," *Pattern Recognit.*, vol. 29, no. 1, pp. 51–59, 1996.
- [30] G. Xu, H.-Z. Wu, and Y. Q. Shi, "Ensemble of CNNs for steganalysis: An empirical study," in *Proc. 4th ACM Workshop Inf. Hiding Multimedia Secur.*, 2016, pp. 103–107.
- [31] V. Sedighi and J. Fridrich, "Histogram layer, moving convolutional neural networks towards feature-based steganalysis," *Electron. Imag., Media Watermarking, Secur., Forensics*, vol. 2017, pp. 50–55, Jan. 2017.
- [32] X. He, D. Cai, and P. Niyogi, "Laplacian score for feature selection," in *Proc. 31st Annu. Conf. Neural Inf. Process. Syst. (NIPS)*, 2006, pp. 507–514.
- [33] X. Tan and B. Triggs, "Enhanced local texture feature sets for face recognition under difficult lighting conditions," *IEEE Trans. Image Process.*, vol. 19, no. 6, pp. 1635–1650, Jun. 2010.
- [34] B. Zhang, Y. Gao, S. Zhao, and J. Liu, "Local derivative pattern versus local binary pattern: Face recognition with high-order local pattern descriptor," *IEEE Trans. Image Process.*, vol. 19, no. 2, pp. 533–544, Feb. 2010.
- [35] F. Lu and J. Huang, "An improved local binary pattern operator for texture classification," in *Proc. IEEE Int. Conf. Acoust., Speech Signal Process.*, Mar. 2016, pp. 1308–1311.
- [36] T. Ojala, M. Pietikäinen, and T. Mäenpää, "Multiresolution gray-scale and rotation invariant texture classification with local binary patterns," *IEEE Trans. Pattern Anal. Mach. Intell.*, vol. 24, no. 7, pp. 971–987, Jul. 2002.
- [37] P. Bas, T. Filler, and T. Pevný, "'Break our steganographic system': The ins and outs of organizing BOSS," in *Proc. 13th Int. Workshop Inf. Hiding*, vol. 6958. 2011, pp. 59–70.
- [38] M. Boroumand and J. Fridrich, "Boosting steganalysis with explicit feature maps," in *Proc. 4th ACM Workshop Inf. Hiding Multimedia Secur.*, 2016, pp. 149–157.
- [39] M. Boroumand and J. Fridrich, "Nonlinear feature normalization in steganalysis," in *Proc. 5th ACM Workshop Inf. Hiding Multimedia Secur.*, 2017, pp. 45–54.
- [40] T. G. Dietterich, "Approximate statistical tests for comparing supervised classification learning algorithms," *Neural Comput.*, vol. 10, no. 7, pp. 1895–1923, 1998.
- [41] B. Li, M. Wang, J. Huang, and X. Li, "A new cost function for spatial image steganography," in *Proc. IEEE Int. Conf. Image Process.*, Oct. 2014, pp. 4206–4210.
- [42] S. Tan, H. Zhang, B. Li, and J. Huang, "Pixel-decimation-assisted steganalysis of synchronize-embedding-changes steganography," *IEEE Trans. Inf. Forensics Security*, vol. 12, no. 7, pp. 1658–1670, Jul. 2017.



Bin Li (S'07–M'09–SM'17) received the B.E. degree in communication engineering and the Ph.D. degree in communication and information system from Sun Yat-sen University, Guangzhou, China, in 2004 and 2009, respectively.

He was a Visiting Scholar with the New Jersey Institute of Technology, Newark, NJ, USA, from 2007 to 2008. In 2009, he joined Shenzhen University, Shenzhen, China, where he is currently an Associate Professor. He is also a member with the Guangdong Key Laboratory of Intelligent Information Processing and the Shenzhen Key Laboratory of Media Security. His current research interests include image processing, multimedia forensics, and pattern recognition.



Zhongpeng Li received the B.E. degree in electronic information engineering and the M.S. degree in information and communication engineering from Shenzhen University, Shenzhen, China, in 2013 and 2017, respectively.

His current research interests include image processing and machine learning.



Shijun Zhou received the B.E. degree in communication engineering from Guizhou University, Guiyang, China. She is currently pursuing the M.S. degree in information and communication engineering from Shenzhen University, Shenzhen, China.

Her current research interests include image steganalysis and forensics.



Shunquan Tan (M'10–SM'17) received the B.S. degree in computational mathematics and applied software and the Ph.D. degree in computer software and theory from Sun Yat-sen University, Guangzhou, China, in 2002 and 2007, respectively.

He was a Visiting Scholar with the New Jersey Institute of Technology, Newark, NJ, USA, from 2005 to 2006. He is currently an Associate Professor with the College Of Computer Science and Software Engineering, Shenzhen University, China. He is also a member with the Shenzhen Key Laboratory of Media Security. His current research interests include steganography, steganalysis, multimedia forensics, and deep machine learning.



Xiaoling Zhang is currently pursuing the B.E. degree in electronic information engineering from Shenzhen University, Shenzhen, China.

Her research interests include steganalysis, steganography, and deep learning.